Optical and Quantum Electronics (2021) 53:368
https://doi.org/10.1007/s11082-021-03013-8

Simulated performance of a novel solid-state dye-sensitized solar cell based on phenyl-C_{61}-butyric acid methyl ester ($PC_{61}BM$) electron transport layer

Benjamin K. Korir[1] · Joshua K. Kibet[1] · Silas M. Ngari[1]

Received: 3 December 2020 / Accepted: 6 June 2021 / Published online: 1 July 2021

Abstract
Climate change has approached a major crisis limit worldwide due to exhaust emissions arising from the use of traditional transport fuels. Solar energy, therefore, appears to be the most promising alternative energy that can mitigate air quality and environmental degradation. Herein, we report numerical simulation of a novel model solid-state dye-sensitized solar cell consisting of solid-state layers with the configuration FTO/PC_{61}BM/N719/CuSCN/Au using 1-dimensional solar cell capacitance simulator software (SCAPS-1D). The motivation underpinning the numerical simulation of the solar cell architecture proposed in this study was to optimize phenyl-C61-butyric acid methyl ester (PC_{61}BM) performance as the electron transport layer. In this model, the effects of varying several parameters—temperature, absorber thickness, defect density, and metallic back contact on the overall solar cell performance have been critically examined. After optimizing the input parameters, the optimal conversion efficiency was 5.38% while the optimized open-circuit voltage was 0.885 V. Besides, 70.94% was the optimum fill factor and the peak short-circuit current of 8.563 mA cm^{-2} was achieved. Built-in voltage of ~1.0 V was estimated from the Mott–Schottky curve and the cell band diagram. The power conversion efficiency obtained in this study is robust for this cell configuration, and is toxic-free compared to the lead-based perovskite solar cells. These findings are therefore useful in the advancement and fabrication of high-performance dye-based photovoltaic devices for large-scale industrial production.

Keywords Climate change · Solar energy · SCAPS-1D · Dye-sensitized solar cells · Numerical simulation

1 Introduction

The current world has witnessed massive environmental degradation as a result of exhaust emissions occasioned by the use of traditional transport fuels such as fossil fuels, coal, and petroleum gases (Wang et al. 2017). Therefore, renewable energy resources

✉ Joshua K. Kibet
jkibet@egerton.ac.ke

[1] Department of Chemistry, Egerton University, P.O BOX 536-20115, Njoro, Kenya

such as solar power and biodiesel that are known to mitigate environmental impacts have lately attracted intense research attention (Korir et al. 2020). In designing solar cells of practical importance, theoretical simulation efforts have been advanced towards sustainable energy alternatives, energy security, and pollution reduction (Gustavsson et al. 2017). Theoretical simulations complement experimental data, save time, and reduce costs in cell design and fabrication. Solar energy is a very promising energy alternative to any renewable or non-renewable energy sources currently available. The energy capacity from the sun in 1.5 days is approximate 1.7×10^{22} J—equivalent to the energy that can be extracted from three trillion barrels of all finite oil reserves in the earth's crust (Crabtree and Lewis 2007). Statistics have shown that the annual consumption of energy worldwide is more than 4.6×10^{20} J, which is the sun's energy amount in one hour (Crabtree and Lewis 2007). Energy from the sun is not only inexhaustible but also environmentally benign. The earth receives 1.2×10^{7} watts from the sun in one day and this energy can meet the world's energy demands required for approximately 20 years (Chu and Meisen 2011). The exponential growth in the human population, advances in industrial systems, human and environmental health, promotion of quality living standards, and climate change has advanced the need for sustainable energy resources (Caruso et al. 2020). Thus, the development of solar infrastructure is projected to address the world's energy demand in the future—in line with millennium sustainable development goals (Santika et al. 2019).

The (DSSCs) have attracted intense interest among research communities because of their attractive features—low toxicities, ease of fabrication, inexpensive cost of materials, good incident photon conversion efficiency (IPCE), flexibility, and good light-harvesting efficiency (LHE) under diffuse conditions (Gong et al. 2017). Generally, DSSCs are manufactured using a liquid electrolyte as an acceptor-type layer (Lee et al. 2017) and an *n*-type layer—the electron transport layer (ETL), which has a photoactive layer anchored onto its surface. Dye-sensitized solar cell (DSSC) consists of five main components: (i) electrolyte (ii) semiconductor (iii) counter electrode (iv) transparent conductive oxide layer (TCO) and (v) photosensitizer as presented in Fig. 1. Previous research findings have reported that the use of liquid state redox electrolytes in dye-based PV cells has posed challenges such as compromised stability of the electrolyte, sublimation, and evaporation of iodine/tri-iodide electrolytes (Dissanayake et al. 2017). Therefore, all-solid-state layers in the cell device

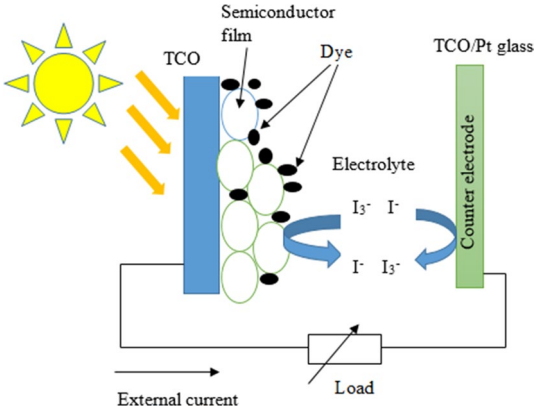

Fig. 1 Schematic diagram showing the main components of DSSCs (Gong et al. 2017)

help overcome the challenges encountered by using iodine/triiodide liquid electrolytes which is not only corrosive but also sublimes.

Solid hole transport layers (HTLs) have been used in DSSCs because of their outstanding merits over the iodine/iodide system; no leakage of charge and no solvent volatility, thus facilitating long-term stability the device (Manfredi et al. 2014). Several HTLs used are less corrosive and thermally stable and include inorganics, *p*-conducting molecules, and organic polymers (Calio et al. 2016). To overcome the challenges of liquid electrolytes, organic and inorganic HTLs have been explored, although their efficiencies are still very low in addition to sealing-related problems (Syafiq et al. 2020).

Over the past decades, TiO_2 material has been the most reasonable ETL finding numerous applications in PV devices with perovskite and dye photoactive layers with better cell performance. Still, it has been reported that it degrades with time due to prolonged Uv-illumination and the presence of oxygen vacancies, leading to activation of surface traps (Madan et al. 2020). Accordingly, there is a need to explore new materials that can be suitable ETLs in thin-film technology. Alternatives that have been studied as ETL materials are $PC_{61}BM$, tin dioxide (SnO_2), tungsten trioxide (WO_3), carbon 60 (C-60), and Zinc oxide (ZnO) (Almeida 2020; Zainudin et al. 2019; Nath et al. 2016; Vittal and Ho 2017).

Previous studies have reported solid-state dye-sensitized solar cell (ssDSSCs) modeled with the N719 photoactive material, TiO_2 mesoporous photoanode, and caesium tin iodide ($CsSnI_3$) as an HTL with direct bandgap having a hole mobility of 585 $cm^2\ V^{-1}\ s^{-1}$ and 1.3 eV bandgap energy (Shum et al. 2010). The cell achieved a PCE of 8.5% and the highest record of photocurrent (J_{sc}) in ssDSSCs of 19.2 mA cm^{-2} (Shum et al. 2010). However, the cell was found to be unstable with time due to the oxidation-induced degradation of $CsSnI_3$ under ambient conditions (Shum et al. 2010). Organic hole conducting materials such as poly(3-hexylthiophe) (P3HT) and poly(3-octylthiophene) (POT) that were initially used in fabricating ssDSSCs showed PCE less than 1% owing to the inadequate filling of pores of the polymer HTLs into the mesoporous TiO_2 film resulting in inefficient separation of charge besides low efficiencies in charge extraction (Lancelle-Beltran et al. 2008). With the optimization of TiO_2 parameters such as porosity, layer thickness, and architecture, a ssDSSC with a TiO_2/N719 dye/P3OT/Au configuration was reported with an efficiency of 1.3% with good stability (Lancelle-Beltran et al. 2006). Research findings have also indicated that the inorganic layer CuSCN does not easily decompose to SCN^{-1}, stoichiometrically large quantities of SCN-1 do not create surface traps in CuSCN. The simulated ssDSSCs based on CuSCN are therefore more stable with useful lifetimes in addition to the most stable open circuit-voltage (V_{oc}) (Perera and Tennakone 2003). The ssDSSCs fabricated by employing TiO_2 as ETL and CuSCN as HTL were found to have a PCE of 2%—attributed to low hole conductance characteristics (O'Regan et al. 2002).

The $PC_{61}BM$ is known to be a comparatively feasible electron acceptor layer (Sun et al. 2014). For instance, the cell configuration with ITO/PEDOT: PSS/CH3NH3PbI$_3$/Al with $PC_{61}BM$ being the ETL gave typical current–voltage (J–V) characteristics of a PV module with a fill factor (FF) of 0.671%, PCE (η) of 3.33%, 5.961 mA cm^{-2} as the short-circuit current (J_{sc}), and 0.832 V as the open-circuit voltage (V_{oc}) (Sun et al. 2014). On the other hand, the perovskite that did not contain $PC_{61}BM$ showed no meaningful photovoltaic characteristics. Therefore, $PC_{61}BM$ has a higher electron affinity as well as a good electron acceptor. A ssDSSC fabricated with the configuration TiO_2/N719dye/$PC_{61}BM$/P3HT yielded a low

cell performance of 1.43% at standard test conditions (STCs) of 100 mW cm^{-2} and AM 1.5 solar spectrum (Yue et al. 2011). The P3HT/$PC_{61}BM$ heterojunction layer transfers carriers and harvests photons from the sun, consequently improving the photoelectric response of DSSCs (Yue et al. 2011). The dye-based PV configuration simulated herein is based on the $PC_{61}BM$ electron transport compact layer.

The effect of changing the photoactive material's density of defects of the photovoltaic conversion efficiency of a typical ssDSSC explored in this work is presented. Moreover, the effects of varying the back metal contact and the operating temperature are examined. The Nyquist plot, Mott Schottky curve, energy band diagram, and optical absorption graphs of the proposed PV configuration are also presented in this work. The solar cell parameters reported in this study are; the fill factor (FF), open-circuit voltage (V_{oc}), power conversion efficiency (PCE), and short circuit current density (J_{sc}). Generally, this study's results are projected to be more useful in the future fabrication and engineering of robust dye-based solar cells that are toxic-free and have longer lifetimes. Although the solar cell under investigation has relatively small power conversion efficiency, it can largely operate at practical temperatures in the range of 260–300 K, implying that it can be installed almost anywhere in the world. This work is envisaged to provide useful findings for the fabrication of high-performance dye-based solar cells which can be injected into the production workflow.

2 Numerical simulation methodology

Computational modelling techniques have been applied in photovoltaic (PV) technology to critically understand their working principles (Rouway et al. 2020). Nonetheless, it is important to elucidate the mechanical, optical, and electrical properties and how these microscopic parameters affect complex solar cell systems (Messmer et al. 2018). This study involves computational electronics using SCAPS-1D 3.3.08 code. The SCAPS-1D package is a numerical software developed at the department of electronics and information systems (ELIS) by Professor Marc Burgelman and his co-workers at the University of Gent, Belgium (Burgelman et al. 2013). When this software is launched, a new window—"action panel" is displayed. This panel contains the "working platform" and also the "action menu" (Jhuma et al. 2019). To carry out simulations, one needs to click on the "set problem," which opens up in a new window. The new window allows for the construction of solar cell layers based on specific input parameters. After constructing the solar cell, the precise measurements to be conducted are specified; current–voltage (I–V), current–voltage (C–V), current–frequency (C–f) and quantum efficiency (QE). By clicking on the "single-shot," the code calculates the specified measurements. The input parameters used in this study are derived from experimental data. The performance of the proposed cell architecture is optimized by making reasonable estimates on layer thickness, temperature variation, and defect densities.

The SCAPS-1D has been employed under the air mass (AM 1.5G) at 1000 Wm^{-2} to investigate current–voltage (J–V) PV characteristics of ssDSSCs. The computer package gives recombination models; auger recombination, radiative recombination, and Shockley–Read–Hall (SRH). In DSSCs, the SHR recombination model is dominant, and it usually occurs when electrons are trapped in an energy state in the forbidden region of the cell. SCAPS-1D has proven to be a powerful tool for simulating thin-film PV module electrical properties with heterojunction technologies (HJT), in which basic semiconductor equations are solved (Movla 2014; Burgelman et al. 2004). The major semiconductor equations are

the continuity and the Poisson. Equation 1 is the Poison equation, whereas Eq. 2 is the continuity equation for electron carriers, while Eq. 3 is the continuity equation for hole carriers. Equation 4 is the drift and diffusion equation for electron carrier, whereas Eq. 5 is the drift and diffusion equation for hole carrier in the conductor (Sobayel et al. 2018).

$$\frac{d^2\emptyset}{dx^2} = \frac{q}{\in_{o\in_r}} p(x) - n(x) + Nd - Na + \rho p - \rho n \tag{1}$$

where Ø(x), ϵ_0, ϵ_r, q, p(x), n(x), Nd, Na, ρp, ρn, vacuum permittivity, relative permittivity, electric charge, hole concentration, electron concentration, charge impurities of donor, charge impurities acceptor, holes distribution and electron distribution, respectively.

$$\frac{dJ\mathrm{n}}{dx} = G - R \tag{2}$$

where Jn represents the current density of electrons, R describes the rate, whereas G describes the rate of electron generation.

$$\frac{dJ_p}{dx} = G - R \tag{3}$$

where Jp is the hole current density, R and G, describes the rates of hole regeneration and generation, respectively.

The transports of the hole and electron carriers in a semiconductor material occur by both drift and diffusion, respectively as;

$$J_{n=}D_{n\frac{dn}{dx}} + \mu_n n\frac{d\emptyset}{dx} \tag{4}$$

$$J_{P=D_p}\frac{dp}{dx} + \mu_p\, p\frac{d\emptyset}{dx} \tag{5}$$

where Dn, Dp, μ_n and μ_p are the electron diffusion coefficient, the hole diffusion coefficient, electron mobility, and hole mobility of holes, respectively.

3 Results and discussion

The ssDSSC employed in the simulation study is a planar heterojunction n–i–p 1-dimensional cell structure. The architecture is FTO/PC_{61}BM/N719/CuSCN/Au where; FTO is fluorine-doped tin oxide, PCBM is the electron acceptor layer, N719 dye is the photoactive layer—di-tetrabutylammonium *cis*-bis(isothiocyanato)bis(2,2′-bipyridyl-4,4′-dicarboxylato)ruthenium(II), CuSCN is copper (I) thiocyanate, and gold (Au) is the back contact. The structural assembly of the cell is shown in Fig. 2a. The n-region is the ETL layer (PC_{61}BM), while the i-layer is the intrinsic region (N719 dye) which is the photoactive layer, and the p-region is the HTL (CuSCN). Upon illumination, the electron–hole pairs are created in the photoactive layer (N719 dye)—Fig. 2b. At the i–p interface, the excitons are dissociated, and holes move to the p region while the remaining electrons diffuse to the *n*-type region. Similarly, in the n–i interface, the excitons are dissociated, and

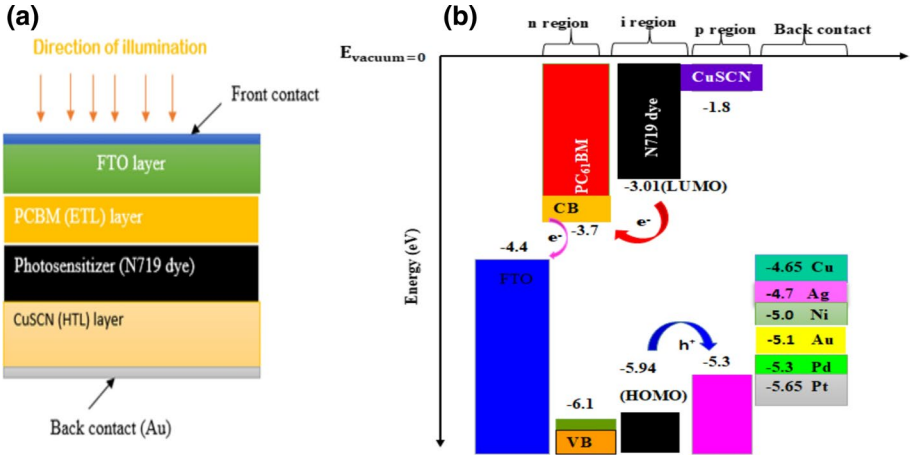

Fig. 2 **a** Device structure of the n–i–p primary dye-based solar cell and **b** band alignment—electron transport layer, and the proposed hole transport layers

the electrons move to the n junction while the remaining holes shift to the *p*-type region. The movement mechanism of excitons is summarized in Fig. 2b.

A ssDSSCs can be modelled in the numerical simulator by constructing a stack of various semiconductor layers described by defect densities, the bandgap energies, the donor densities, the electron affinities, doping, or changing material's physical parameters, and the thickness of materials (Decock et al. 2012). The simulated device contains all solid layers and input parameters of varying thickness, bandgap energy (E_g), the electron affinity (χ), acceptor density (N_A), relative dielectric permittivity (ϵ/ϵ_r), the donor density (N_D), defect densities N_t, mobility of electrons (μ_e), hole electron mobility (μ_p), conduction band densities (N_C) and the valence band densities (N_V). The interface defect properties of the CuSCN/N719 dye are summarized in Table 1.

The selected input parameters used in this study were extracted from literature from experimental data presented in Table 2. The optimum defect density (N_t) of PCBM and HTL–CuSCN considered in this study was 2.0×10^{17} cm^{-3} and 1.0×10^{22} cm^{-3}, respectively.

Upon simulation, the 1-dimensional solar cell capacitance simulator (SCAPS-1D) computational code gives the illuminated J–V characteristic curve unique for particular cell architecture. It provides an efficient way of obtaining the photovoltaic performance

Table 1 The interface defects properties of the CuSCN/N719 dye interface

Defect type	Neutral
Capture cross section electrons (cm^2)	1.00×10^{-19}
Capture cross-section of holes (cm^2)	1.00×10^{-19}
Energetic distribution	Single
Reference for defect energy level Et	Above the highest eV
The energy with respect to Reference (eV)	0.600
Total density (integrated over all energies) (1/cm^2)	1.00×10^{12}

Table 2 Material properties applied in the simulation of the model solar cell device (Rondan-Gómez et al. 2020; Jahantigh and Safikhani 2019; Rai et al. 2020; Gan et al. 2020; Azri et al. 2019; Zhang et al. 2014)

	FTO	PCBM	N719 dye	CuSCN
Thickness (nm)	400	30	6000.00	200
Band-gap energy (eV)	3.50	2.0	2.33	3.60
Electron affinity (eV)	4.00	3.90	3.90	1.70
Relative permittivity(e_r)	9.00	3.90	30.00	10.00
Effective density of conduction band N_C (cm^{-3})	9.20×10^{18}	2.2×10^{21}	2.40×10^{20}	1.00×10^{21}
Effective density of valence band N_V (cm^{-3})	1.80×10^{19}	2.2×10^{21}	2.50×10^{20}	1.00×10^{21}
The thermal velocity of electrons (cm/Vs)	1.00×10^{7}	1.00×10^{7}	1.00×10^{7}	1.00×10^{7}
The thermal velocity of holes (cm/Vs)	1.00×10^{7}	1.00×10^{7}	1.00×10^{7}	1.00×10^{7}
Electron mobility (cm^2/s)	20	0.2	5.00	100.00
Hole mobility (cm^2/s)	10	0.2	5.00	25.00
Density of acceptors (cm^{-3})	0.00	0.00	1.00×10^{17}	1.00×10^{17}
The density of donors (cm^{-3})	1.00×10^{19}	2.93×10^{17}	0.00	0.00
Total density N_t ($1/cm^3$)	–	2.0×10^{17}	–	1.00×10^{22}

of a solar cell. Figure 2a, vide supra, shows the simulated solid-state dye-sensitized solar cell's architecture with illumination incident on the front contact, entering the FTO, then the PCBM (ETL), absorber N719 dye, and finally through the hole transport layer (HTL)–CuSCN.

3.1 Quantum efficiency of the model solar cell

The QE studies of a PV cell are characterized by external quantum efficiency (EQE) and internal quantum efficiency (IQE). The IQE is the ratio of the electron–hole pairs generated to the total number of absorbed photons also called quantum yield whereas the EQE is defined as the ratio of the collected charge carriers to number of irradiating photons on a PV device (Karmalawi et al. 2020). Figure 3 shows the EQE (%) of the simulated ssDSSCs

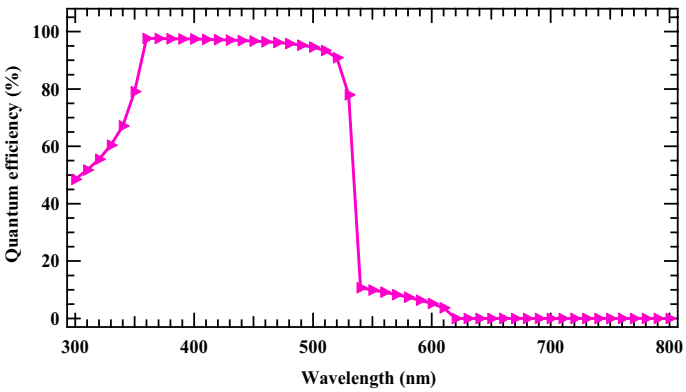

Fig. 3 External quantum efficiency (EQE) of the cell as a function of the photon wavelength

explored in this work. The EQE of the device rises from 48.5% at 300 nm to a maximum of 97.6% at 370 nm but gradually decreases to 3.80% at approximately 610 nm. Typical dyes such as N719 have intense absorption spectra from ultra-violet to near-infrared thus making them highly desirable in DSSCs for optimal LHE. The N719 pigment absorbs solar radiance over the wavelength range of 300–900 nm owing to the transitions in metal-to-ligand charge transfer (Aghazada and Nazeeruddin 2018; Barrera et al. 2016). However, this dye is affected by low molecular coefficients that often result in intramolecular charge transfer within the same wavelength range. Nonetheless, the LHE of N719 dye-based ssDSSCs can be optimized by co-sensitizing N719 dye with organic dyes such as triphenylamines (Sharma et al. 2013; Wu et al. 2014).

The spectrum (cf. Fig. 3) describes how solar radiance is converted into electricity as a function of measured wavelengths (Markvart and Castañer 2013) and is consistent with the optimum absorption spectrum of N719 dye (Han et al. 2010). For a general PV cell, the IPCE (QE) in most cases exhibits "square-like" plots as the value of IPCE largely remains constant over the wavelengths measured (300–900 nm) (Ranjusha et al. 2011). The photoactive material (N719 dye) used in this study exhibits good electron affinity—converting nearly all of the absorbed photons into usable energy in the range 360–520 nm, and exhibiting relatively good compatibility with other semiconductor materials (*n* and *p*-type layers). However, from this study, it can be noted that energy losses due to charge carrier recombination before collection at the external circuit. The dye can absorb more photons that are efficiently photo-converted into electricity, but its EQE decreases gradually longer wavelengths. At approximately 610 nm, the cell becomes inefficient due to the inability of the absorber to absorb photons of longer wavelengths because of the high rate of charge recombination.

The quantum efficiency (QE) can be expressed as a function of wavelength. Equation 6 gives the relation between QE and J_{sc}

$$J_{sc} = q \int \emptyset(\lambda) QE(\lambda) d(\lambda) \tag{6}$$

From Eq. 6, $\emptyset(\lambda)$ is the photon flux per wavelength.

3.2 Effect of CuSCN/N719 interface defects

Figure 4 shows the modelled cell configuration using various semi-conductor layers for the simulated solid-state dye-sensitized solar cell reported in this study. The defects at the CuSCN/N719 interface were also considered in this work. At the top right of Fig. 4, the measurement specified for the numerical simulation include direction of illumination, direction of voltage applications, and current reference settings.

Previous studies have shown that the quality of the junction interface is critical in the overall performance of a solar cell architecture (Gan et al. 2020). High defect densities increase the rate of charge recombination besides decreasing the quality of the PV layers (Devi et al. 2018). As can be noted in Table 3, the performance of the ssDSSCs decreased when the density of defects at the interface was increased. This is associated with increased recombination centers and the availability of more surface traps. This is consistent with previous studies reported in literature (Gan et al. 2020).

Fig. 4 The constructed stack of layers for the simulated ssDSSCs in SCAPS-1D code

Table 3 The J–V characteristics of the simulated solar cell when the CuSCN/719 dye interface defect densities is varied

Defect densities on CuSCN/N719 interface ($1/cm^2$)	Voc (V)	J_{sc} (mA cm^{-2})	FF (%)	PCE (%)
1.00×10^1	0.9704	8.924	67.18	5.82
1.0×10^3	0.9704	8.924	67.18	5.82
1.0×10^5	0.9704	8.924	67.18	5.82
1.0×10^7	0.963	8.909	67.57	50.80
1.0×10^9	0.900	8.656	70.54	5.50
1.0×10^{10}	0.8875	8.578	70.90	5.40
1.0×10^{12}	0.885	8.563	70.94	5.38

3.3 Current–voltage (J–V) characteristics

The output of the simulation calculations under AM1.5 at 100Wcm^{-2} gave the results;V_{oc} = 0.885 V, J_{sc} = 8.563 mA cm^{-2}, FF = 70.94% and PCE = 5.38%. The value of V_{oc} (0.885 V), is the peak voltage at which current flows in the external circuit when the terminals of the ssDSSCs are not connected. This is the optimal voltage the PV device can produce. The value of (V_{oc}) is dependent on the photogenerated current density. The J_{sc} (8.563 mA cm^{-2}) refers to the current produced by the solar cell in the presence of illumination when the solar cell terminals are in contact with each other (short-circuited). The FF (70.94%) is defined as the ratio between maximum obtainable power to the product of (V_{oc}) and the (J_{sc}) generated by the ssDSSCs. This parameter is useful in describing the quality of the photovoltaic device (Bartesaghi et al. 2015). The fill factor (FF) describes the "squareness" of the current–voltage (J–V) curve characteristics as presented in Fig. 5a. The

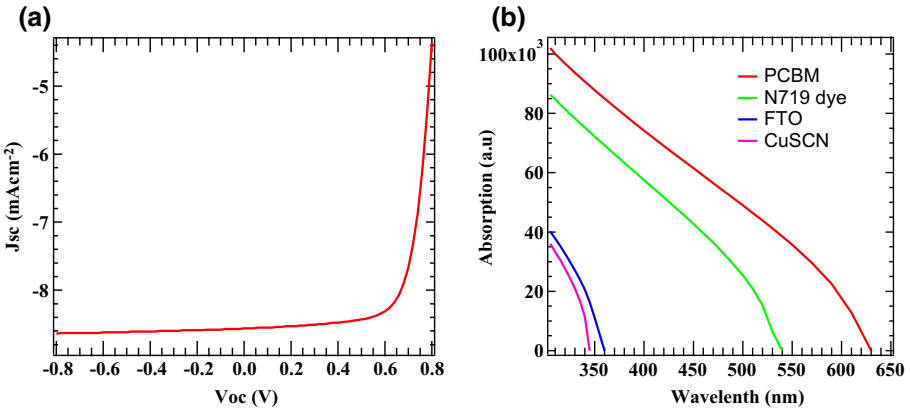

Fig. 5 The J–V characteristics **a** and **b** the optical absorption of the simulated PV device

absorption graph of the proposed device is presented in Fig. 5b. The value of PCE is calculated as the ratio of maximum power P_{max} and incident power P_{in} as expressed in Eq. 7. The current recombination curves show the rate of recombination of hole carriers (h^+) and electron carriers (e^-) during the photo-conversion of incident photons by the solar cell.

The absorption efficiencies of the layers of the simulated ssDSSCs as a function of wavelength are presented in Fig. 5b. As reported in Fig. 5b, the layers; PCBM, CuSCN, FTO, and N719 have different absorption coefficients and have varying abilities in the absorption of photons. The layer with the highest absorption coefficient (PCBM) absorbs photons more readily. These photons get excited into the conduction band of the semiconductor. The absorption coefficients show how light of a given wavelength penetrates into the solar device before it is absorbed (Kabir et al. 2019). Wavelengths with lower energies than band gap energies lack adequate energies that can excite an electron from the valence band into the conduction band. The HTL–CuSCN has very low absorption power and therefore a poor absorber of photons compared to the layer with high absorption coefficient—PCBM (cf. Figure 5b). The expression showing the relationship between the extinction coefficient and the absorption coefficient is given by Eq. 7;

$$\alpha = 4\pi k \frac{1}{\lambda} \tag{7}$$

where α, k, and λ is absorption coefficient, extinction coefficient and wavelength of photons in (nm), respectively (Kabir et al. 2019). The value of α is multiplied by 10^7 and the absorption coefficient is given in cm^{-1}.

3.4 Effect of temperature

The prevailing temperature conditions in a given environment plays a significant role in the performance of ssDSSCs (Kim et al. 2015). Solar cell devices are usually installed outdoors; over time, they get affected by peak temperatures, especially during summer, leading to the degradation of their thermal stabilities (Kersten et al. 2015). Generally, solar cells operate at temperatures above 300 K (Sobayel et al. 2018). However, the present third-generation solar cells are also efficient under diffuse conditions and can be installed

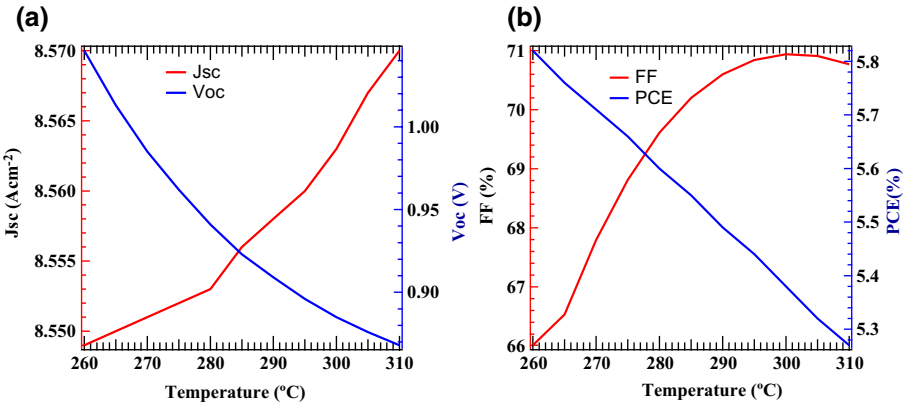

Fig. 6 Temperature effects on **a** J_{sc} and V_{oc}, **b** FF and PCE

on windows (Reynaud et al. 2019). Therefore, it is necessary to investigate the effect of temperature variation on cell performance. In this study, the temperature in the range of 260–310 K was investigated. The output in Fig. 6a illustrates that both the short circuit current (J_{sc}) increased and the open-circuit voltage (V_{oc}) decreased as the working temperature is increased from 260 to 300 K. As presented in Fig. 6b the PCE gradually decreased as the FF increased when the temperature is varied from 260 to 300 K. Increasing the temperature reduces the semiconductor useful lifetimes. Notably, PV devices are unstable at high temperatures hence these devices degrade and hence their performances are compromised (Lim et al. 2021).

The expression for efficiency of a solar cell device is given by Eq. 8;

$$\mathrm{PCE} = \frac{P_{max}}{P_{in}} = \frac{V_{oc} \times J_{sc} \times \mathrm{FF}}{P_{in}} \times 100\%. \tag{8}$$

Expression 9 gives the relationship of FF, V_{oc} and J_{sc};

$$\mathrm{FF} = \frac{\mathrm{Pmax}}{V_{oc} \times J_{sc}} = \frac{\mathrm{Jmp} \times \mathrm{Vmp}}{\mathrm{Voc} \times \mathrm{JSC}}. \tag{9}$$

As can be observed in Fig. 6b, when the temperature is increased from 260 to 310 K, there is a gradual increase in short circuit current, (J_{sc}) from 8.549 to 8.57 mA cm^{-2}. This increase is associated with a decrease in the recombination of charge at the heterojunction barrier when the thermal activation energy increases as a result of increase in temperature. It is also noted that the V_{oc} decreases from 1.046 to 0.868 V when the temperature rises from 260 to 300 K. This decrease is attributed to an increase in the value of dark saturation current J_0 and ultimately high rates of carrier charge recombination. The V_{oc} depends on J_{SC}, as predicted by Eq. 10;

$$V_{oc} = \frac{nk_BT}{q} \ln\left[\frac{J_{sc}}{J_o} + 1\right] \tag{10}$$

where J_{sc} is the photogenerated current in the presence of light illumination, J_0 is the dark saturation current, T is the absolute temperature in Kelvins (K), k_B is the Boltzmann constant ($k_B = 1.38 \times 10^{-23}$ JK^{-1}), q is the electronic charge $\left(q = 1.603 \times 10^{-19}\ C\right)$ and n,

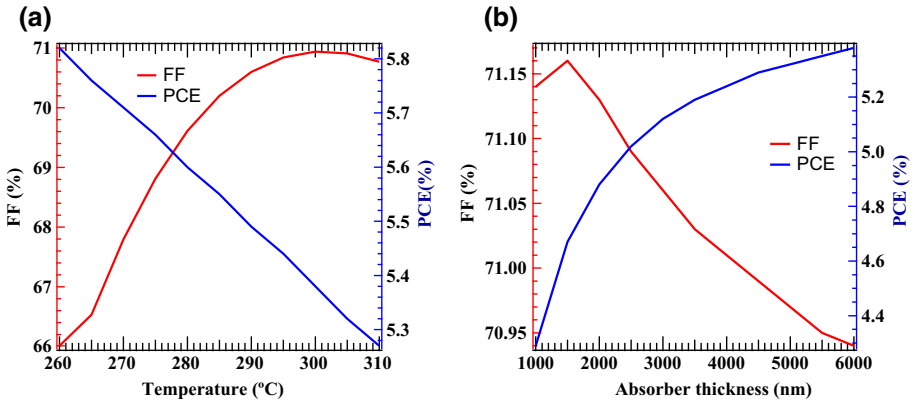

Fig. 7 Variation in absorber thickness with **a** J_{sc} and V_{oc}, **b** FF and PCE

$(1 < n > 2)$ as the ideality factor. The term $\frac{nk_BT}{q}$ gives the thermal voltage or flow of elementary current.

The diffusion length of the charge carriers due to the photosensitizer plays an important role in determining the solar performance of the solar cell device (Kaiser et al. 2001). An increase in defect densities increases the rate at which charge carriers recombine. This problem can be minimized using a thicker absorber layer comparable with the depletion layer thickness (Kaiser et al. 2001). Figure 7a illustrates that when the thickness of the dye is increased from 1000 to 6000 nm, the overall cell efficiency starts to increase. It can be noted that the efficiency increases from 4.29% at 1000 nm to 5.38% when the absorber thickness layer is increased to 6000 nm. A thin absorber layer only absorbs fewer incident photons, but as the layer thickness is increased, the PCE increases because more photons are absorbed hence the performance of the cell approaches an optimum value. On the other hand, the FF gradually increases from 71.14 to 71.16% as the absorber layer thickness is increases from 1000 to 1500 nm and then decreases to 70.94% as the absorber layer thickness increases from1500–6000 nm.

3.5 Absorber layer thickness

The performance of ssDSSCs is dependent on the thickness of the photosensitizer—in this case, N719 dye. The dye is responsible for absorbing photons that are converted at the p-i-n junction of the cell into electricity (Xiang et al. 2019). The pigments that are used in PV technology should absorb solar radiance within the visible and near-infrared (IR) regions of the spectrum (300–900 nm) (Cai et al. 2019). Absorber layer thickness has a remarkable influence on V_{oc} PCE, FF, and J_{sc}. In this work, the absorber thickness was varied from 1000 to 6000 nm using the SCAPS-1D computational code. The output in Fig. 7a indicates that the J_{sc} gradually increase as the absorber layer thickness increases. At 6000 nm, the J_{sc} reaches a maximum value of 8.885 mA cm^{-2} whereas the power conversion efficiency increases gradually and attains a maximum of 5.38%. Thicker layers of the absorber absorb more photons, resulting in the generation

of electron–hole pairs (e^- h^+ pairs). When the absorber layer thickness is 1500 nm, V_{oc} and J_{sc} are relatively lower (0.869 V and 7.557 mA cm^{-2}, respectively) due to the incomplete absorption of incident photons (Mohamed 2014). The power conversion efficiency at this thickness (1500 nm) is significantly low—4.29%. This can be attributed to the recombination of charge carriers (photogenerated charge) at the back contact, usually positioned near the depletion region in the cell and the short diffusion length of the photosensitizer. These observations are consistent with other studies in literature (Yang et al. 2018).

3.6 Effect of CuSCN and FTO thickness

The FTO and HTL play critical roles in the overall performance of the cell in the optimization of PCE and photo-thermal stabilities. Increasing the thickness of CuSCN from 100 to 1000 nm, the cell parameters; FF, PCE, V_{oc},J_{sc} remained constant at 70.94%, 5.38%, 0.885 V, and 8.563 mA cm^{-2}, respectively. This shows that the HTL is equally efficient at all the simulated thickness and can combine with the N719 dye more effectively. On the other hand, increasing the FTO thickness from 100 to 1000 nm, the PCE gradually decreased from 5.44 to 5.31%. The FF remained constant from 100 to 700 nm layer thickness but increased to 70.95% when the thickness increased from 800 to 1000 nm. Accordingly, thicker FTO layers show good chemical and thermal stabilities besides providing high electrical conductivity and optical transparency thus becoming highly attractive for use in ssDSSCs (Huang et al. 2009).

Table 4 The out parameters V_{oc}, J_{sc} FF and PCE when CuSCN and FTO thickness are varied

Thickness in (nm)	Material	V_{oc} (V)	J_{sc} (mA cm^{-2})	FF (%)	PCE (%)
100	FTO	0.886	8.655	70.94	5.44
	CuSCN	0.885	8.563	70.94	5.38
200	FTO	0.886	8.619	70.94	5.42
	CuSCN	0.885	8.563	70.94	5.38
300	FTO	0.886	8.589	70.94	5.4
	CuSCN	0.885	8.563	70.94	5.38
400	FTO	0.885	8.563	70.94	5.38
	CuSCN	0.885	8.563	70.94	5.38
500	FTO	0.885	8.541	70.94	5.36
	CuSCN	0.885	8.563	70.94	5.38
600	FTO	0.885	8.521	70.94	5.32
	CuSCN	0.885	8.563	70.94	5.38
700	FTO	0.885	8.504	70.94	5.34
	CuSCN	0.885	8.563	70.94	5.38
800	FTO	0.885	8.489	70.95	5.33
	CuSCN	0.885	8.563	70.94	5.38
900	FTO	0.885	8.475	70.95	5.32
	CuSCN	0.885	8.563	70.94	5.38
1000	FTO	0.885	8.463	70.95	5.31
	CuSCN	0.885	8.563	70.94	5.38

As presented in Table 4, increasing the thickness of FTO from 100 to 1000 nm decreases the (V_{oc}) values from 0.886 to 0.855 V while the photo-generated current (J_{sc}) decreased from 8.655 to 8.463 mA cm^{-2}. A decrease in (V_{oc}) is attributed to an increase in the rate of recombination of charge carriers and an increase in dark saturation current, J_0. On the other hand, a decrease in open-circuit voltage, (V_{oc}), and photogenerated current (J_{sc}) increases the fill factor (FF) (cf. Table 4). The optimum thickness of FTO is 100 nm. This is the thickness range at which the cell has good power conversion efficiency (PCE) of 5.44%, high V_{oc} value (0.886 V) and J_{sc} value (8.655 mA cm^{-2}).

3.7 Effect of the back contact work function

The electrical properties of the back contact are very important in the performance of photovoltaic devices. Molybdenum (Mo) has been a good back contact material in thin-film PV systems. Nonetheless, it has not been the best alternative because of its low power conversion efficiency (Altamura et al. 2014). Gold (Au) has proven to be the best performing back contact material although its application has been impeded by high cost and the fact that the atoms of Au diffuse to other solar cell layers, thus compromising its performance (Teixeira et al. 2019). To demonstrate the potential of the best performing, cheap, and reliable back contact, we investigated the performance of ssDSSCs by varying the metal back contact—having different metal work functions. The simulated materials were; copper (Cu), Au, nickel (Ni), platinum (Pt), Silver (Ag), and palladium (Pd)—Table 5. The metal front contact is selected to be flat bands and the SCAPS-1D software is able to automatically give the work function of the metal.

As can be observed in Table 5, the performance of the cell is increased when higher metal work functions of the back contacts are used. Similarly, the FF values increases at high metal work function of the back contact, which also translates to increased power conversion efficiency as shown in Table 5. Evidently, from the results reported in this work, the noble back contact metals include Au, Ni, Pt, and Pt. These metal back-contacts are competitive for use in solar cells. Gold (Au) and Pt are very expensive back contact materials (Hall et al. 2021). As can be noted from Table 5, the preferred material to be used as the metal back contact in the simulated ssDSSCs is Ni owing to its competitive performance. Compared to palladium and other metal back contacts, nickel is readily available in nature, cheap, has a higher work function, reliable and exhibits good power conversion performance (cf. Table 5).

Table 5 The ssDSSCs cell performance characteristics for different metal back contacts

Back contact metal work function	V_{oc}	J_{sc} (mA cm^{-2})	FF (%)	PCE (%)
Copper (4.65)	0.881	8.562	70.39	5.31
Silver (4.7)	0.885	8.563	70.85	5.37
Nickel (5.0)	0.885	8.563	70.94	5.38
Gold (5.1)	0.885	8.563	70.94	5.38
Palladium (5.3)	0.885	8.563	70.94	5.38
Platinum (5.65)	0.885	8.563	70.94	5.38

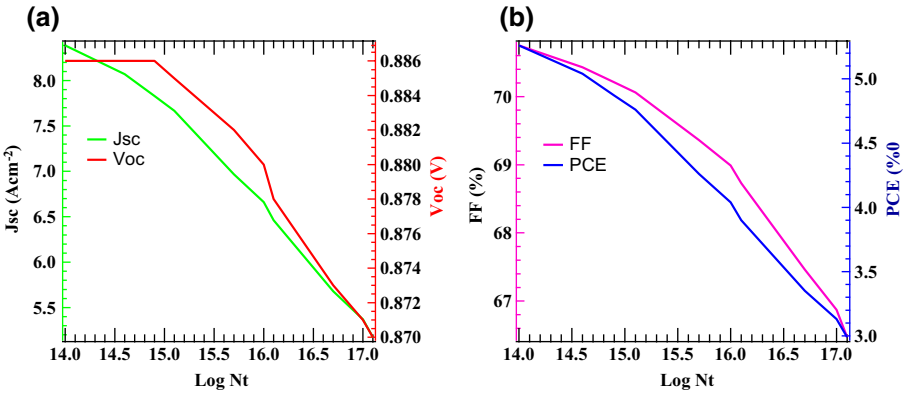

Fig. 8 The effect of absorber defect density with Jsc and Voc **a** and **b** PCE and FF as a function absorber defect density

3.8 Effect of absorber defect densities and PCBM donor densities

In this work, the effect of N719 dye defect densities (N_t) on the performance of the proposed model PV device was also investigated. It is evident that increasing the concentration of defect densities results in the decrease of the overall performance of the solar cell device. Besides, increasing the concentration of the defects on the absorber layer—N719 dye from 1.00×10^{14} cm^{-3}, the, J_{sc} decreased from 8.386 to 5.174 mA cm^{-2} at a defect density concentration of 1.33×10^{17} cm^{-3}. In contrast, the Voc remained approximately constant (0.886 V) when Nt is increased from 1.0×10^{14} to 2.0×10^{15} cm^{-3} then falls gradually to 0.87 V when the concentration of Nt is increased to 1.33×10^{17} cm^{-3}. Figure 8a shows the plot of J_{sc} and V_{oc} as a function of Log N_t. From Fig. 8b, the value of PCE decreased from 5.26 to 2.99% whereas the FF decreased from and 70.75 to 66.47% when the concentration of Nt was increased from 1.00×10^{14} cm^{-3} to 1.33×10^{17} cm^{-3}. At 1.00×10^{14} cm^{-3}, the PCE of the device was 5.26% and at the concentrations of 1.33×10^{17} cm^{-3}, the value of the PCE of the device decreased to 2.99%. Also, the FF of the device decreased from 70.75% at 1.00×10^{14} cm^{-3} as the concentration of the absorber defects increased. Notably, at a high defect concentration of 1.33×10^{17} cm^{-3}, the FF is 66.47%. The plot of FF (%) and PCE (%) as a function of Log N_t is presented in Fig. 8b.

The performance of the ssDSSCs was also investigated by controlling the concentration of the acceptor donors. When the concentration of donor densities (N_D) of PCBM is 2.00×10^{15} cm^{-3}, the cell has an overall efficiency of 5.17%. When the concentration of N_D of PCBM is gradually increased, the cell performance rises to 5.44% at 1.00×10^{17} cm^{-3}. The efficiency of the cell decreases to 5.26% when the concentration of N_D is 7.00×10^{17} cm^{-3}. On the other hand, FF increases from 70.57 to 70.96% when the concentration of N_D is 2.00×10^{15} cm^{-3} and 1.00×10^{17} cm^{-3}, respectively. The FF then decreases to 58.22% when the concentration of N_D is increased to 7.00×10^{17} cm^{-3}. The V_{oc} gradually increases (0.862–1.057 V) when the concentration of the N_D of the ETL–PCBM increases from 2.00×10^{15} cm^{-3} to 7.00×10^{17} cm^{-3}. As can be witnessed in Fig. 9a, the plots of J_{sc}, and V_{oc} as a function of Log N_D, the J_{sc} and V_{oc} steadily increased as the concentration of N_D is increased but the J_{sc} sharply decreased when the concentration of N_D was increased to 7.00×10^{17} cm^{-3}. The values of PCE (Fig. 9b)

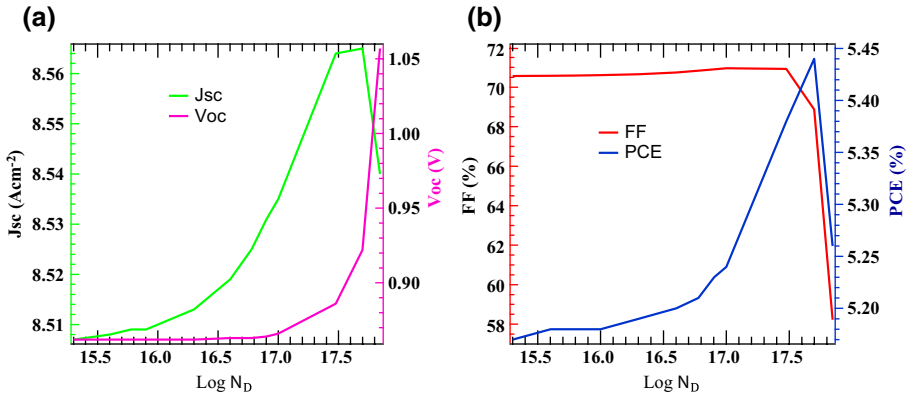

Fig. 9 Variation of Log N_D with (a) J_{sc} and V_{oc} (**a**) FF and PCE and (**b**)

increased as the concentrations of the secondary dopants increased, but the FF values remained approximately constant when the concentration of N_D was increased from 2.00×10^{15} cm^{-3}–3.00×10^{17} cm^{-3} but sharply decreased when the value of donor density concentration (N_D) increased to 7.00×10^{17} cm^{-3}. The optimum donor density N_D on the PCBM layer is 5.0×10^{17} cm^{-3} with a PCE of 5.44%, 8.565 mA cm^{-2} as the peak J_{sc}, FF of 68.87%, and V_{oc} of 0.922 V.

3.9 Heterojunction and conductance-voltage (G-V) characteristics

At the *p*–*n* junction of a heterojunction cell, the charge-carriers diffuse across to either layer thus creating a depletion region with a corresponding potential V_{ib}. This is referred to as built-in voltage given by Eq. 11.

$$V_{ib} = E_{g2} - (E_f - E_{C2}) + X_2 - X_1 - (E_{C1} - E_f) \tag{11}$$

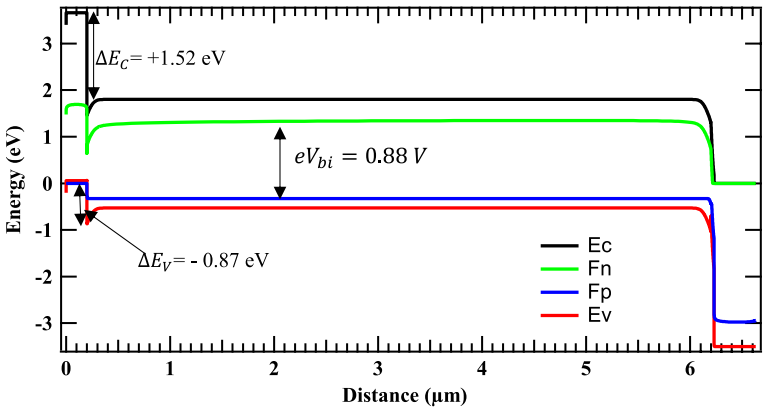

Fig. 10 Band energy diagram of ssDSSCs at equilibrium

where E_g, X, E_C and E_f are bandgap energy, electronic affinities of semiconductor material, conduction band level and Fermi level, respectively. Figure 10 presents ssDSSCs band energy diagram where; $\Delta E_v = \Delta E_C + \Delta E_g$ and the component ΔE_g designates the bandgap energy of the material. As ascribed at the heterojunction, ΔE_C jump from conduction bands of the n-type and p-type semiconductors is attributed to the difference in their electron affinities. From Fig. 10, the value of ΔE_V is − 0.87 eV, implying an energy barrier to charge collection in the *p*-type layer of holes is created when the *n*-type layer is illuminated. On the other hand, the value of ΔE_C is + 1.52 eV, indicating that there is no energy barrier towards the collection of electrons by the n-type layer generated by the *p*-type layer under illumination. The eV_{bi} (0.88 V) is the built-in voltage and is obtained by considering the Eq. 12;

$$eV_{bi} = EF_n - EF_p \tag{12}$$

From the SCAPS-1D code, a solar device impedance can be measured under varied frequencies, typically 1 MHz to below 0.1 Hz. Arguably, the characterization of impedance in solar cells is presented by the Nyquist plot, Fig. 11a. It is used to describe both the imaginary (*y*-axis) and real parts (*x*-axis) of impedance (Z). This plot is useful in describing the dependence of solar cell performance on operating frequency and voltage. The operating voltage is dependent on the amount of PV ability to absorb the maximum number of photons. From the Nyquist plot, both the imaginary and real parts relate to the inverse of capacitance and conductance, respectively, which is consistent with experimental and theoretical studies previously reported in literature (Bouzidi et al. 2020).

Figure 11b shows the conductance–voltage (G–V) characteristics. The G–V plots are useful in characterizing the densities of interface states. The present study was conducted at a frequency of 10^5 Hz. The conductance represents energy losses due to the capture and emission of charge carriers by the interface traps. The curve presents interface states and traps in the interface states by considering a constant time of carrier capture with its corresponding energy position.

Characterization of capacitance–voltage measurements has been widely used to describe the density of charge carriers and as well as explain anomalies in interface states, deep levels, and also non-uniformities in polycrystalline and amorphous materials (Hailegnaw et al. 2020).

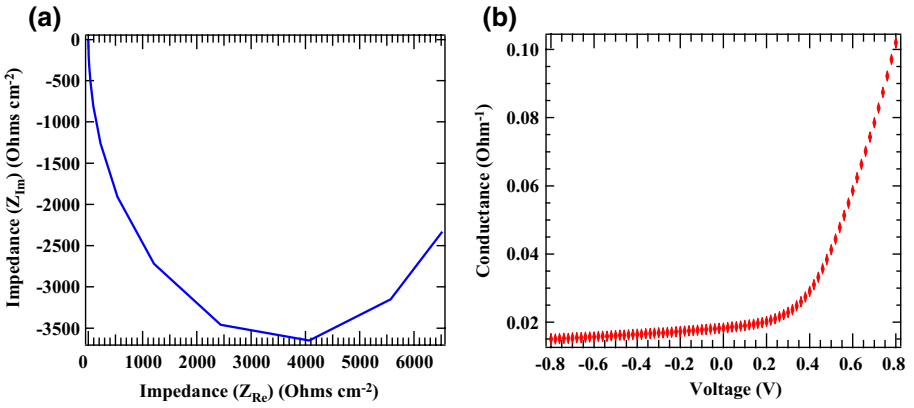

Fig. 11 Imaginary impedance as a function of real impedance **a** and **b** conductance as a function of voltage

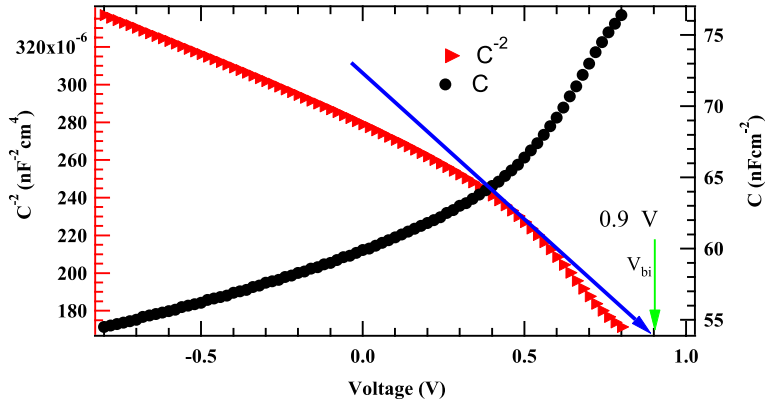

Fig. 12 Mott–Schottky curve of the simulated ssDSSCs derived from C–V characteristics

Figure 12 gives the Mott–Schottky plot of the simulated ssDSSCs. From the plot, it is possible to obtain the charge density distribution by using the expression 13;

$$N_C(W) = \frac{2}{qK_S\epsilon_0 \; A^2\left[\frac{d\left(1/C^2\right)}{dv}\right]} \tag{13}$$

where $N_C(W)$, ϵ_0, A, q, K_S and $\frac{d\left(1/C^2\right)}{dv}$ are; charge density, permittivity of free space, surface area, electron charge, relative permittivity, and the Mott-Schottky slope, respectively. The voltage modulation in the depletion region and C-V measurements represented by the Mott-Schottky analysis gives the built-in voltage and the photoactive layer acceptor defect densities (Almora et al. 2016). Besides, the variation of alternating current (AC) helps in the derivation of the drive-level capacitance profile (DLCP) (Eisenbarth et al. 2010). The value of the V_{bi} obtained from the Mott Schottky curve (0.9 V) is approximately the same as the value obtained from the energy band diagram, 0.88 V, and is consistent with literature findings (Olusola et al. 2018).

Table 6 compares various cell parameters arising from the use of various materials as electron transport compact layers. Whereas previous work on dye-based sensitized solar cells used inorganic TiO_2 as the ETL, this work uses an organic material, PCBM, and still achieves robust power conversion efficiency (PCE).

The present simulation results provide critical information on how parameters can be varied for the actual fabrication of ssDSSCs with remarkable performance. The proposed PCBM as ETL has good semiconductor properties—good electron acceptor and high electron affinity which is ideal for solar cell designs and fabrication. The HTL layer (CuSCN) does not decompose to SCN^{-1}; hence the cell device is stable, toxic-free, and has better cell lifetimes. The simulation results presented in Table 4 are an important guide in comparing organic and inorganic HTLs for improving the parameters of conductive polymers with secondary doping, and fabricating optimized SDSSCs for manufacturing workflow to allow for its large-scale production (Teixeira et al. 2019).

Table 6 The photovoltaic (J–V) characteristics of various ssDSSCs cell configurations

Device architecture	Experimental/Simulation	V_{oc} (V)	J_{sc} (mA cm^{-2})	FF (%)	PCE (%)	References
ITO/PEN/TiO_2/N719 dye/PCBM/P3HT	Experimental	0.87	3.0	0.54	1.43	Yue et al. (2011)
FTO/TiO_2/BEHP-co-MEH PPV/PEDOT: PSS/Pt	Simulation (SCAPS-1D)	1.53	6.43	80.58	7.95	Rondan-Gómez et al. (2020)
FTO/TiO2/Sb_2S_3/N719/CuI	Experimental	0.371	13.4	0.503	2.5	Dematage (2014)
ITO/CuSCN/P3HT/P3HT: PCBM/Al	Experimental	0.56	7.70	0.57	2.6	Takahashi et al. (2007)
FTO/TiO_2/BEHP-co-MEH PPV/MoO2MoO_3/Pt	Simulation (SCAPS-1D)	2.14	4.23	92.93	8.42	Rondan-Gómez et al. (2020)
FTO/TiO2/N719/modified CuSCN/carbon past/Pt-FTO	Experimental	0.647	15.76	0.416	4.24	Dematage (2014)
FTO/PC_{61}BM/N719 dye/CuSCN/Au	Simulation (SCAPS-1D)	0.885	8.563	70.94	5.38	This work

4 Conclusions

In this paper, numerical simulation of ssDSSCs has been carried out using SCAPS-1D software. The overall cell performance was optimized by making reasonable adjustments on thickness, working temperature, N719 dye thickness, carrier densities, and various material defect density. The optimum PCE of the solar cell designed in this study was 5.38%, which is relatively robust compared to different solar cell architecture designs reported in previous experimental and theoretical studies. The optimal lowest working temperature of this device is 260 K, with a PCE of 5.82%, V_{oc} of 1.046 V, FF 66.01%, and J_{sc} is 8.549 mA cm^{-2}. This demonstrates that the model solar cell can operate at various energy demands during winter and other low-temperature climates. The optimized power conversion efficiency was 5.38% at 300 K—suitable for humid subtropical climates in Latin America and Africa. This study has also established that Ni back contact can replace Au, Pt, Ag, or Pd as back metals because it gives similar power conversion efficiency and is less expensive than gold, silver, platinum and palladium, besides being readily available. Moreover, simulation of the cell design proposed in this work has also demonstrated that the optimum thickness of the N719 layer is between 5000 and 6000 nm at an optimum working temperature of 300 K, whereas the optimal PCBM thickness is 30 nm. The best working thickness range for FTO is 100–300 nm, while that of the HTL (CuSCN) is 200–1000 nm. Accordingly, solar energy has the potential to promote energy security if the fabrication conditions are properly controlled. Numerical simulation of solar cell designs saves on time and cost by providing critical information to solar cell manufacturers. Nevertheless, an experimental approach to the model ssDSSCs photovoltaic cell performance is recommended in order to complement the theoretical work reported in this study.

Acknowledgements The authors wish to thank Prof. Marc Burgelman of the department of electronics and information systems (ELIS), Gent University—Belgium, for providing us with the SCAPS-1D license used for numerical simulations reported in this work. Mr. Rono of the University of KwaZulu-Natal is highly appreciated for his advice and input towards the success of this manuscript.

Funding The authors are grateful to Egerton University Grant #EU/RE/DVC/072 for facilitating this research.

Declaration

Conflict of interests The authors have no competing interests.

References

Aghazada, S., Nazeeruddin, M.K.: Ruthenium complexes as sensitizers in dye-sensitized solar cells. Inorganics **6**(2), 52 (2018). https://doi.org/10.3390/inorganics6020052

Almeida, M.A.: Recent advances in solar cells. In: Solar Cells, pp. 79–122. Springer (2020). doi: https://doi.org/10.1007/978-3-030-36354-3_4

Almora, O., Aranda, C., Mas-Marzá, E., Garcia-Belmonte, G.: On Mott–Schottky analysis interpretation of capacitance measurements in organometal perovskite solar cells. Appl. Phys. Lett. **109**(17), 173903 (2016). https://doi.org/10.1063/1.4966127

Altamura, G., Grenet, L., Roger, C., Roux, F., Reita, V., Fillon, R., Fournier, H., Perraud, S., Mariette, H.: Alternative back contacts in kesterite Cu2ZnSn (S1-xSex) 4 thin film solar cells. J. Renew. Sustain. Energy **6**(1), 011401 (2014). https://doi.org/10.1063/1.4831781

Azri, F., Meftah, A., Sengouga, N., Meftah, A.: Electron and hole transport layers optimization by numerical simulation of a perovskite solar cell. Sol. Energy **181**, 372–378 (2019). https://doi.org/10.1016/j.solener.2019.02.017

Barrera, M., Crivelli, I., Loeb, B.: On the performance of ruthenium dyes in dye sensitized solar cells: a free cluster approach based on theoretical indexes. J. Mol. Model. **22**(5), 118 (2016). https://doi.org/10.1007/s00894-016-2984-2

Bartesaghi, D., del Carmen Pérez, I., Kniepert, J., Roland, S., Turbiez, M., Neher, D., Koster, L.J.A.: Competition between recombination and extraction of free charges determines the fill factor of organic solar cells. Nat. Commun. **6**(1), 1–10 (2015). https://doi.org/10.1038/ncomms8083

Bouzidi, A., Jilani, W., Yahia, I., Zahran, H.: Impedance spectroscopy of monocrystalline silicon solar cells for photosensor applications: highly sensitive device. Physica B **596**, 412375 (2020). https://doi.org/10.1016/j.physb.2020.412375

Burgelman, M., Decock, K., Khelifi, S., Abass, A.: Advanced electrical simulation of thin film solar cells. Thin Solid Films **535**, 296–301 (2013). https://doi.org/10.1016/j.tsf.2012.10.032

Burgelman, M., Verschraegen, J., Degrave, S., Nollet, P.: Modeling thin-film PV devices. Prog. Photovoltaics Res. Appl. **12**(2–3), 143–153 (2004). https://doi.org/10.1002/pip.524

Cai, W., Zhang, Z., Jin, Y., Lv, Y., Wang, L., Chen, K., Zhou, X.: Application of TiO2 hollow microspheres incorporated with up-conversion NaYF4: Yb3+, Er3+ nanoparticles and commercial available carbon counter electrodes in dye-sensitized solar cells. Sol. Energy **188**, 441–449 (2019). https://doi.org/10.1016/j.solener.2019.05.081

Calio, L., Kazim, S., Graetzel, M., Ahmad, S.: Hole-transport materials for perovskite solar cells. Angew. Chem. Int. Ed. **55**(47), 14522–14545 (2016). https://doi.org/10.1002/anie.201601757

Caruso, G., Colantonio, E., Gattone, S.A.: Relationships between renewable energy consumption, social factors, and health: a panel vector auto regression analysis of a cluster of 12 EU countries. Sustainability **12**(7), 2915 (2020). https://doi.org/10.3390/su12072915

Chu, Y., Meisen, P.: Review and comparison of different solar energy technologies. Global Energy Network Institute (GENI), San Diego (2011)

Crabtree, G.W., Lewis, N.S.: Solar energy conversion. Phys. Today **60**(3), 37–42 (2007). https://doi.org/10.1063/1.161619

Decock, K., Zabierowski, P., Burgelman, M.: Modeling metastabilities in chalcopyrite-based thin film solar cells. J. Appl. Phys. **111**(4), 043703 (2012). https://doi.org/10.1063/1.3686651

Dematage, N.: Dye-sensitized and Semiconductor-sensitized Solid State Solar Cells Utilizing CuSCN and CuI as Hole Conducting Materials. In: 静岡大学, (2014)

Devi, N., Parrey, K.A., Aziz, A., Datta, S.: Numerical simulations of perovskite thin-film solar cells using a CdS hole blocking layer. J. Vac. Sci. Technol. B Nanotechnol. Microelectron. Mater. Process. Meas. Phenom. **36**(4), 04G105 (2018). https://doi.org/10.1116/1.5026163

Dissanayake, M.L., Senadeera, G., Bandara, T.: Mixed cation effect and iodide ion conductivity in electrolytes for dye sensitized solar cells. Ionics **23**(10), 2901–2907 (2017). https://doi.org/10.1007/s11581-016-1902-z

Eisenbarth, T., Unold, T., Caballero, R., Kaufmann, C.A., Schock, H.-W.: Interpretation of admittance, capacitance-voltage, and current-voltage signatures in Cu (In, Ga) Se 2 thin film solar cells. J. Appl. Phys. **107**(3), 034509 (2010). https://doi.org/10.1063/1.3277043

Gan, Y., Bi, X., Liu, Y., Qin, B., Li, Q., Jiang, Q., Mo, P.: Numerical investigation energy conversion performance of tin-based perovskite solar cells using cell capacitance simulator. Energies **13**(22), 5907 (2020). https://doi.org/10.3390/en13225907

Gong, J., Sumathy, K., Qiao, Q., Zhou, Z.: Review on dye-sensitized solar cells (DSSCs): advanced techniques and research trends. Renew. Sustain. Energy Rev. **68**, 234–246 (2017). https://doi.org/10.1016/j.rser.2016.09.097

Gustavsson, L., Haus, S., Lundblad, M., Lundström, A., Ortiz, C.A., Sathre, R., Le Truong, N., Wikberg, P.-E.: Climate change effects of forestry and substitution of carbon-intensive materials and fossil fuels. Renew. Sustain. Energy Rev. **67**, 612–624 (2017). https://doi.org/10.1016/j.rser.2016.09.056

Hailegnaw, B., Sariciftci, N.S., Scharber, M.C.: Impedance spectroscopy of perovskite solar cells: studying the dynamics of charge carriers before and after continuous operation. Phys. Stat. Solidi A **217**(22), 2000291 (2020). https://doi.org/10.1002/pssa.202000291

Hall, R.S., Lamb, D., Irvine, S.J.C.: Back contacts materials used in thin film CdTe solar cells—a review. Energy Sci. Eng. (2021). https://doi.org/10.1002/ese3.843

Han, J., Fan, F., Xu, C., Lin, S., Wei, M., Duan, X., Wang, Z.L.: ZnO nanotube-based dye-sensitized solar cell and its application in self-powered devices. Nanotechnology **21**(40), 405203 (2010). https://doi.org/10.1088/0957-4484/21/40/405203

Huang, X., Zhang, Y., Sun, H., Li, D., Luo, Y., Meng, Q.: A new figure of merit for qualifying the fluorine-doped tin oxide glass used in dye-sensitized solar cells. J. Renew. Sustain. Energy **1**(6), 063107 (2009). https://doi.org/10.1063/1.3278518

Jahantigh, F., Safikhani, M.J.: The effect of HTM on the performance of solid-state dye-sanitized solar cells (SDSSCs): a SCAPS-1D simulation study. Appl. Phys. A **125**(4), 276 (2019). https://doi.org/10.1007/s00339-019-2582-0

Jhuma, F.A., Shaily, M.Z., Rashid, M.J.: Towards high-efficiency CZTS solar cell through buffer layer optimization. Mater. Renew. Sustain. Energy **8**(1), 6 (2019). https://doi.org/10.1007/s40243-019-0144-1

Kabir, F., Sakib, S.N., Matin, N.: Stability study of natural green dye based DSSC. Optik **181**, 458–464 (2019). https://doi.org/10.1016/j.ijleo.2018.12.077

Kaiser, I., Ernst, K., Fischer, C.-H., Könenkamp, R., Rost, C., Sieber, I., Lux-Steiner, M.C.: The eta-solar cell with CuInS2: a photovoltaic cell concept using an extremely thin absorber (eta). Sol. Energy Mater. Sol. Cells **67**(1–4), 89–96 (2001). https://doi.org/10.1016/S0927-0248(00)00267-1

Karmalawi, A.M., Rayan, D.A., Rashad, M.M.: Establishment and evaluation of photovoltaic quantum efficiency system at central metallurgical research and development institute. Optik **217**, 164931 (2020). https://doi.org/10.1016/j.ijleo.2020.164931

Kersten, F., Engelhart, P., Ploigt, H.-C., Stekolnikov, A., Lindner, T., Stenzel, F., Bartzsch, M., Szpeth, A., Petter, K., Heitmann, J.: Degradation of multicrystalline silicon solar cells and modules after illumination at elevated temperature. Sol. Energy Mater. Sol. Cells **142**, 83–86 (2015). https://doi.org/10.1016/j.solmat.2015.06.015

Kim, J.H., Moon, K.J., Kim, J.M., Lee, D., Kim, S.H.: Effects of various light-intensity and temperature environments on the photovoltaic performance of dye-sensitized solar cells. Sol. Energy **113**, 251–257 (2015). https://doi.org/10.1016/j.solener.2015.01.012

Korir, B.K., Kibet, J.K.,Mosonik, B.C.: A review of the current trends in the production and consumption of bioenergy (2020). https://doi.org/10.22034/pcbr.2021.126117

Lancelle-Beltran, E., Prené, P., Boscher, C., Belleville, P., Buvat, P., Lambert, S., Guillet, F., Marcel, C., Sanchez, C.: Solid-state organic/inorganic hybrid solar cells based on poly (octylthiophene) and dye-sensitized nanobrookite and nanoanatase TiO2 electrodes. Eur. J. Inorg. Chem. **2008**(6), 903–910 (2008). https://doi.org/10.1002/ejic.200701033

Lancelle-Beltran, E., Prené, P., Boscher, C., Belleville, P., Buvat, P., Sanchez, C.: All-solid-state dye-sensitized nanoporous TiO2 hybrid solar cells with high energy-conversion efficiency. Adv. Mater. **18**(19), 2579–2582 (2006). https://doi.org/10.1002/adma.200502023

Lee, C.-P., Li, C.-T., Ho, K.-C.: Use of organic materials in dye-sensitized solar cells. Mater. Today **20**(5), 267–283 (2017). https://doi.org/10.1016/j.mattod.2017.01.012

Lim, J., Kim, M., Park, H.H., Jung, H., Lim, S., Hao, X., Choi, E., Park, S., Lee, M., Liu, Z.: Kinetics of light-induced degradation in semi-transparent perovskite solar cells. Sol. Energy Mater. Sol. Cells **219**, 110776 (2021). https://doi.org/10.1016/j.solmat.2020.110776

Madan, J., Garg, S., Gupta, K., Rana, S., Manocha, A., Pandey, R.: Numerical simulation of charge transport layer free perovskite solar cell using metal work function shifted contacts. Optik **202**, 163646 (2020). https://doi.org/10.1016/j.ijleo.2019.163646

Manfredi, N., Bianchi, A., Causin, V., Ruffo, R., Simonutti, R., Abbotto, A.: Electrolytes for quasi solid-state dye-sensitized solar cells based on block copolymers. J. Polym. Sci. Part A Polym. Chem. **52**(5), 719–727 (2014). https://doi.org/10.1002/pola.27055

Markvart, T. , Castañer, L.: Chapter IA-1-principles of solar cell operation. Sol. Cells 3–25 (2013). https://doi.org/10.1016/B978-0-12-809921-6.00001-X

Messmer, C., Bivour, M., Schön, J., Glunz, S.W., Hermle, M.: Numerical simulation of silicon heterojunction solar cells featuring metal oxides as carrier-selective contacts. IEEE J. Photovoltaics **8**(2), 456–464 (2018). https://doi.org/10.1109/JPHOTOV.2018.2793762

Mohamed, H.: Theoretical study of the efficiency of CdS/PbS thin film solar cells. Sol. Energy **108**, 360–369 (2014). https://doi.org/10.1016/j.solener.2014.07.017

Movla, H.: Optimization of the CIGS based thin film solar cells: numerical simulation and analysis. Optik **125**(1), 67–70 (2014). https://doi.org/10.1016/j.ijleo.2013.06.034

Nath, N.C.D., Choi, S.Y., Jeong, H.W., Lee, J.-J., Park, H.: Stand-alone photoconversion of carbon dioxide on copper oxide wire arrays powered by tungsten trioxide/dye-sensitized solar cell dual absorbers. Nano Energy **25**, 51–59 (2016). https://doi.org/10.1016/j.nanoen.2016.04.025

O'Regan, B., Lenzmann, F., Muis, R., Wienke, J.: A solid-state dye-sensitized solar cell fabricated with pressure-treated P25–TiO2 and CuSCN: analysis of pore filling and IV characteristics. Chem. Mater. **14**(12), 5023–5029 (2002). https://doi.org/10.1021/cm020572d

Olusola, O., Ewetumo, T., Obagade, T.,Adedayo, K.: Electronic behaviour of schottky diodes fabricated from electroplated CdSe semiconductors. Asian J. Res. Rev. Phys. 1–8 (2018). https://doi.org/10.9734/ajr2p/2018/v1i224603

Perera, V., Tennakone, K.: Recombination processes in dye-sensitized solid-state solar cells with CuI as the hole collector. Sol. Energy Mater. Sol. Cells **79**(2), 249–255 (2003). https://doi.org/10.1016/S0927-0248(03)00103-X

Rai, N., Dwivedi, D.: Numerical modelling for enhancement of output performance of CIGS based thin film solar cell using SCAPS 1-D simulation software. In: AIP Conference Proceedings. Vol. 1, p. 140021. AIP Publishing LLC (2020). https://doi.org/10.1063/5.0001233

Rai, N., Rai, S., Singh, P.K., Lohia, P.,Dwivedi, D.: Analysis of various ETL materials for an efficient perovskite solar cell by numerical simulation. J. Mater. Sci. Mater. Electron. 1–12 (2020). doi: https://doi.org/10.1007/s10854-020-04175-z

Ranjusha, R., Lekha, P., Subramanian, K., Shantikumar, V.N., Balakrishnan, A.: Photoanode activity of ZnO nanotube based dye-sensitized solar cells. J. Mater. Sci. Technol. **27**(11), 961–966 (2011). https://doi.org/10.1016/S1005-0302(11)60170-9

Reynaud, C.A., Clerc, R., Lechêne, P.B., Hébert, M., Cazier, A., Arias, A.C.: Evaluation of indoor photovoltaic power production under directional and diffuse lighting conditions. Sol. Energy Mater. Sol. Cells **200**, 110010 (2019). https://doi.org/10.1016/j.solmat.2019.110010

Rondan-Gómez, V., Ayala-Mató, F., Seuret-Jiménez, D., Santana-Rodríguez, G., Zamudio-Lara, A., De Los Santos, I.M., Seuret-Hernández, H.: New architecture in dye sensitized solar cells: a SCAPS-1D simulation study. Opt. Quant. Electron. **52**(6), 1–11 (2020). https://doi.org/10.1007/s11082-020-02437-y

Rouway, M., Boulahia, Z., Chakhchaoui, N., Fouzia, F., Omari, L.E.H., Cherkaoui, O.,Van Langenhove, L.: Mathematical and numerical modelling of soiling effects of photovoltaic solar panels on their electrical performance. In: IOP Conference Series: Materials Science and Engineering. Vol. 1, p. 012064. IOP Publishing (2020). https://doi.org/10.1088/1757-899X/827/1/012064

Santika, W.G., Anisuzzaman, M., Bahri, P.A., Shafiullah, G., Rupf, G.V., Urmee, T.: From goals to joules: a quantitative approach of interlinkages between energy and the sustainable development goals. Energy Res. Soc. Sci. **50**, 201–214 (2019). https://doi.org/10.1016/j.erss.2018.11.016

Sharma, G., Singh, S.P., Kurchania, R., Ball, R.: Cosensitization of dye sensitized solar cells with a thiocyanate free Ru dye and a metal free dye containing thienylfluorene conjugation. RSC Adv. **3**(17), 6036–6043 (2013). https://doi.org/10.1039/C3RA23155K

Shum, K., Chen, Z., Qureshi, J., Yu, C., Wang, J.J., Pfenninger, W., Vockic, N., Midgley, J., Kenney, J.T.: Synthesis and characterization of CsSnI 3 thin films. Appl. Phys. Lett. **96**(22), 221903 (2010). https://doi.org/10.1063/1.3442511

Sobayel, K., Rahman, K., Karim, M., Aijaz, M., Dar, M., Shar, M., Misran, H.,Amin, N.: Numerical modeling on prospective buffer layers for tungsten di-sulfide (WS_2) solar cells by scaps-1d. Chalcogenide Lett. **15**(6) (2018).

Sun, S., Salim, T., Mathews, N., Duchamp, M., Boothroyd, C., Xing, G., Sum, T.C., Lam, Y.M.: The origin of high efficiency in low-temperature solution-processable bilayer organometal halide hybrid solar cells. Energy Environ. Sci. **7**(1), 399–407 (2014). https://doi.org/10.1039/C3EE43161D

Syafiq, U., Ataollahi, N., Scardi, P.: Progress in CZTS as hole transport layer in perovskite solar cell. Sol. Energy **196**, 399–408 (2020). https://doi.org/10.1016/j.solener.2019.12.016

Takahashi, K., Suzaka, S., Sigeyama, Y., Yamaguchi, T., Nakamura, J.-I., Murata, K.: Efficiency increase by insertion of electrodeposited CuSCN layer into ITO/organic solid interface in bulk hetero-junction solar cells consisting of polythiophene and fullerene. Chem. Lett. **36**(6), 762–763 (2007). https://doi.org/10.1246/cl.2007.762

Teixeira, C.O., Andrade, L., Mendes, A.: Novel carbon-based material for perovskite solar cells back-contact. Int. J. Energy Res. **43**(13), 7541–7546 (2019). https://doi.org/10.1002/er.4695

Vittal, R., Ho, K.-C.: Zinc oxide based dye-sensitized solar cells: a review. Renew. Sustain. Energy Rev. **70**, 920–935 (2017). https://doi.org/10.1016/j.rser.2016.11.273

Wang, J., Feng, L., Tang, X., Bentley, Y., Höök, M.: The implications of fossil fuel supply constraints on climate change projections: a supply-side analysis. Futures **86**, 58–72 (2017). https://doi.org/10.1016/j.futures.2016.04.007

Wu, Z., Wei, Y., An, Z., Chen, X., Chen, P.: Co-sensitization of N719 with an organic dye for dye-sensitized solar cells application. Bull. Korean Chem. Soc **35**(5), 1449 (2014)

Xiang, C., Zhao, X., Tan, L., Ye, J., Wu, S., Zhang, S., Sun, L.: A solar tube: Efficiently converting sunlight into electricity and heat. Nano Energy **55**, 269–276 (2019). https://doi.org/10.1016/j.nanoen.2018.10.077

Yang, Q., Wang, K., Yu, H., Zhu, X., Han, C., Deng, L., Yang, H., Zhao, F., Sun, X., Zhang, Q.: Surface polarization and recombination in organic-inorganic hybrid perovskite solar cells based on photo-and electrically induced negative capacitance studies. Org. Electron. **62**, 203–208 (2018). https://doi.org/10.1016/j.orgel.2018.08.015

Yue, G., Wu, J., Xiao, Y., Ye, H., Lin, J., Huang, M.: Flexible dye-sensitized solar cell based on PCBM/P3HT heterojunction. Chin. Sci. Bull. **56**(3), 325–330 (2011). https://doi.org/10.1007/s11434-010-3080-0

Zainudin, S., Abdullah, H., Markom, M.: Electrochemical studies of tin oxide based-dye-sensitized solar cells (DSSC): a review. J. Mater. Sci. Mater. Electron. **30**(6), 5342–5356 (2019). https://doi.org/10.1007/s10854-019-00929-6

Zhang, J., Yu, C., Wang, L., Li, Y., Ren, Y., Shum, K.: Energy barrier at the N719-dye/CsSnI 3 interface for photogenerated holes in dye-sensitized solar cells. Sci. Rep. **4**(1), 1–6 (2014). https://doi.org/10.1038/srep06954